Materials and Corrosion

Materials and Corrosion

ARTICLE OPEN ACCESS

Effect of Oxygen and Nitrogen Oxide Gas Concentration on Corrosion of 310N Stainless Steel in Solar Salt at 600°C

Sumit Kumar[1] | Srinivasan Swaminathan[2] | Rene Hesse[2] | Wenjin Ding[1] | Thomas Bauer[3]

[1]Institute of Engineering Thermodynamics, German Aerospace Center (DLR), Stuttgart, Baden-Württemberg, Germany | [2]Division 5.1—Microstructural Design and Degradation, Bundesanstalt für Materialforschung Und—Prüfung (BAM), Department of Materials Engineering, Berlin, Germany | [3]Institute of Engineering Thermodynamics, German Aerospace Center (DLR), Cologne, North Rhine-Westphalia, Germany

Correspondence: Sumit Kumar (sumit.kumar@dlr.de)

Received: 12 June 2025 | **Revised:** 24 March 2026 | **Accepted:** 18 April 2026

Funding: Deutsche Forschungsgemeinschaft, Grant/Award Number: 455432503

Keywords: austenitic stainless steel | corrosion mechanism | corrosion mitigation | gas atmosphere effects | high temperature corrosion | salt chemistry | thermal Energy Storage | thermochemical stability

ABSTRACT

Concentrated solar power (CSP) systems commonly use solar salt as a high temperature heat transfer and storage medium. This study examines the effect of oxygen (O_2) and nitrogen oxide (NO) gas concentrations on solar salt thermal stability and 310N stainless steel corrosion at 600°C up to 1224 h. The impact of the gas atmosphere (5–80 vol% O_2, 400–600 ppm NO) on salt chemistry, including nitrate, nitrite, oxide, and chromate ions, was analyzed, and corrosion behavior was evaluated through weight change, corrosion rate, and microstructural analysis. The results show that introducing NO gas concentrations $\geq$ 400 ppm with at least 5 vol% O_2 stabilizes salt decomposition by controlling nitrite and oxide ion formation and promotes the development of a protective corrosion layer on the steel surface. Once this protective layer is formed, variations in oxygen concentration (5–80 vol%) in the presence of $\geq$ 400 ppm NO gas have a minimal long-term effect on the corrosion behavior of stainless steel in solar salt. These findings underscore the importance of maintaining minimum O_2 and NO levels to optimize salt chemistry that effectively mitigates steel corrosion in solar salt systems.

1 | Introduction

Use of renewable energy is important for long term and sustainable energy supply. One of the advancements in the renewable energy storage is storing solar radiation as thermal energy in molten salt system coupled with concentrated solar power (CSP) plants and using them later for dispatchable electricity production. Molten salt systems are state-of-the-art technology for CSP applications. Solar salt, which is a non-eutectic mixture of 60 wt% $NaNO_3$ and 40 wt% KNO_3 is used almost exclusively [1]. This salt mixture is primarily used for thermal energy storage (TES), but also as a heat transfer fluid (HTF). While it is widely used in CSP systems, its application is not only limited to this domain. It can also be utilized for high-temperature process heat applications [2].

Solar salt has an operating temperature range of 290°C to 565°C. The upper working temperature limit of solar salt is governed by the thermal stability of solar salt, that is, the thermal decomposition of solar salt is considered to be a several step process. The first and widely understood decomposition reaction is the decomposition of nitrate ion to form nitrite ion and oxygen gas as given by Equation (1) [3–5].

$$NO_3^- \rightleftarrows NO_2^- + \frac{1}{2}O_2(g) \quad (1)$$

The decomposition equilibrium reaction is dependent on the temperature and oxygen vol%. Under typical operating conditions in an air atmosphere with an oxygen gas concentration of 20 vol% at 560°C, an equilibrium nitrite concentration of

4.5 mol% based on anion composition was observed after 500 h [6]. This concentration increased to 8 mol% at 600°C, demonstrating the effect of temperature on nitrite formation [7]. Additionally, at 560°C, increasing the oxygen gas concentration to 50 vol% at ambient pressure led to a decrease in nitrite concentration to 3.1 mol%, highlighting the crucial role of oxygen gas concentration in controlling the nitrate–nitrite decomposition reaction (Equation (1)) [7]. This relation, showing an overall decrease in equilibrium nitrite concentration and increase in nitrate concentration with increasing oxygen vol%, has been summarized by Steinbrecher et al. [8].

It should be noted that at temperatures above 500°C, nitrite ions can further decompose into several decomposition products, such as nitrogen oxide gases, nitrogen gas, and oxide ions [9–12]. However, the exact stoichiometry of the equilibrium decomposition reaction is not fully known, leading to the simplified Equation (2) below.

$$NO_2^- \rightleftarrows N_xO_y(g) + O_a^{b-} \quad (2)$$

In Equation (2), N_xO_y represents various nitrogen oxide gases such as nitrogen oxide (NO), nitrogen dioxide (NO_2) that may form during salt decomposition. The term O_a^{b-} denotes oxide ions such as (O_2^{2-}, O_2^-, O^{2-}) or other oxygen containing anionic species present in the molten salt. Previous research indicates that, in the absence of nitrogen oxide gases, this reaction can proceed in the forward direction, producing more oxide ions and reach up to a value of 0.04 mol% at 600°C after 1000 h [7, 10].

Overall, there is a common consensus that oxide ions present in solar salt at high temperatures accelerate the corrosion of metallic components in contact [13–16]. Several strategies in molten nitrate salt systems have been explored to mitigate corrosion [17], including protective coatings [18, 19], additives or nanoparticles [20, 21], and the control of cover gas to manipulate salt chemistry [22]. Among these approaches, control of the gas atmosphere plays a critical role, as it directly governs salt decomposition and the formation of corrosive oxide species [8]. Our earlier study also demonstrated that the oxide ion concentration increases to 3.5 mol% due to solar salt decomposition in a nitrogen-purged atmosphere with 0 vol% oxygen, leading to a significant increase in the corrosion rate, which is nearly ten times higher compared to that in an air atmosphere with 20 vol% oxygen at 600°C [23]. These previously reported results serve as the control reference for the present study. Earlier studies have also shown that increasing oxide ions by adding sodium peroxide (0.1–1 mol% of Na_2O_2) to nitrate salt or sodium oxide (1 wt% of Na_2O) to nitrate/nitrite salt mixtures significantly increases the corrosion rate of AISI 316 stainless steel above 550°C [24, 25]. In some cases, the corrosion rate is found to increase by up to 30 times for stainless steel, reaching 965 μm/year at 650°C after 14 days, and a similar trend at 530°C [24]. In line with these studies, our recent findings demonstrated that the increase in oxide ions by addition of either sodium oxide (Na_2O) or sodium peroxide (Na_2O_2) in solar salt, above 0.20 wt% (0.25 mol% oxide ion), leads to increased corrosion of 316 L at 600°C in a purged synthetic air atmosphere (20 vol% oxygen). This is accompanied by a corresponding increase in the dissolution of major alloying elements (e.g., Cr) and the formation of a porous, disintegrated corrosion layer as the oxide ion concentration rises [26, 27]. Recent studies have shown that the presence of NO gas even in small amounts can suppress the oxide ion formation in the salt at elevated temperature above 550°C, by stabilizing nitrite decomposition (Equation(2)) [8, 10, 28]. Moreover, Bonk et al. [22] also demonstrated that solar salt decomposition at 620°C, that is, the formation of nitrite and oxide ions can be effectively controlled with a purged gas atmosphere containing 400 ppm nitrogen oxide NO and 80 vol% oxygen. The limited availability of oxide ions due to NO gas leads to slower corrosion reaction kinetics for the formation of the corrosion layer, for example, a sodium iron oxide top layer, and this results in a denser, stable, and non-porous protective corrosion layer on 316 SS, compared to an atmosphere with 20 vol% oxygen [22]. In summary, earlier studies have shown that an oxygen free atmosphere (0 vol% oxygen) increases salt decomposition and higher corrosion rates compared to synthetic air containing 20 vol% oxygen, while 80 vol% oxygen in the presence of NO gas has been found to suppress salt decomposition and further decreases corrosion. Moreover, in current CSP systems, the systems operate under ambient air conditions with approximately 21 vol % O_2. However, it is well established that increasing the oxygen partial pressure stabilizes the solar salt chemistry and reduces its corrosivity [22, 29]. Therefore, precise control of the gas atmosphere represents a promising strategy to further improve the chemical stability and durability of next-generation CSP-TES systems. Despite these advances, to the best of our knowledge there is still a lack of systematic research at a temperature of 600°C on how the oxygen volume fraction influence the solar salt chemistry and also the corrosion rate, particularly in the presence of suppressed oxide ions in the salt melt with NO containing cover gas.

To address the gap, the current study significantly extends the scope by analyzing the impact of both oxygen and NO gas concentration variation on the corrosion of 310N SS in solar salt, compared to previous similar work without variation of the oxygen concentration [22, 28]. Alloy 310N was selected as a representative nitrogen-alloyed, high-chromium and nickel austenitic stainless steel developed for its suitability at higher temperatures with improved resistance to creep strength and corrosion resistance as compared to other grades like 316 and 316 L [30]. The main objective of this study is to examine how corrosion in solar salt is influenced by variations in nitrate and nitrite ion concentrations, which are controlled by adjusting the oxygen vol%, particularly under conditions where NO gas reduces oxide ion formation. For this purpose, the oxygen vol% was varied from 5 vol% to 80 vol%, and NO gas concentrations of 400 and 600 ppm were purged into solar salt containing 310N stainless steel for up to 1224 h. These concentrations were chosen based on the minimum requirement identified by Steinbrecher et al. [31], who showed that 200 ppm NO gas together with 5 vol% O_2 is necessary for salt stabilization, although oxide-ion concentrations still tend to increase under these conditions. Therefore, a higher concentration of 400 ppm NO was selected in the present study to limit any possibility of oxide-ion accumulation, and 600 ppm NO was additionally applied to compare the effect of increasing NO gas concentration. Due to the growing interest in raising the operating temperature of CSP systems beyond 565°C to increase energy storage density and cost reduction, this study investigates the

resulting changes in corrosion behavior and salt chemistry at 600°C. The impact of changing gas atmosphere on both the salt chemistry and the corrosion of 310N stainless steel was analyzed. The salt chemistry was examined for nitrate, nitrite, chromate, and oxide ions. The 310N stainless steel corrosion was evaluated through weight change, mass loss by descaling, and analysis of corrosion layer morphology and cross-sections. Overall, by providing deeper insights into the complex interactions between gas atmosphere, salt chemistry, and steel corrosion, this research offers a path forward for developing corrosion mitigation and optimization strategies, extending the lifespan of stainless-steel components, and reducing operational costs in CSP-TES systems and other high-temperature energy storage applications.

2 | Materials and Methods

The following sections describe the experimental setup (Subsection 2.1), procedure (Subsection 2.2), and post-experimental salt and steel analysis (Subsection 2.3).

2.1 | Experimental Setup

The corrosion study was conducted in a modified convection furnace with four holes on the top of the furnace, designed to securely hold four alumina crucibles. The alumina crucibles are positioned 30 mm outside the furnace to prevent salt creeping, as hot solar salt tends to creep beyond the furnace due to its high temperature. To control the atmosphere inside the crucibles, the top of each alumina crucible is fitted with a stainless-steel flange assembly, with holes for both gas inlet and outlet. The outlet hole of the flange is also used for periodic temperature measurements using a K-type thermocouple. This setup is described in detail elsewhere [14]. To eliminate any possibility of metallic interaction with the solar salt, an alumina sample holder is used to hold the steel samples inside the salt. For precise control of the gas flow, a set of three calibrated mass flow controllers (MFCs) are used for each crucible to regulate the flow of oxygen (grade 5.0, Linde Gas, Germany), nitrogen (grade 5.0, Linde Gas, Germany), and nitrogen oxide (2000 ppm mixed with N_2, Linde Gas, Germany). The total gas flow rate in each crucible is maintained at 100 mL/min. The variation in gas flow composition of each experiments are described in the section below (see Table 2).

2.2 | Procedure

For the corrosion study the solar salt was produced from pro analysis grade $NaNO_3$ (purity > 99.5%, Merck, Germany) and KNO_3 (purity > 99.5%, Merck, Germany) at a 60/40 wt% ratio. The corrosion tests were conducted using AISI 310 N stainless steel (Salzgitter Mannesmann Forschung GmbH (SZMF), Germany), and the chemical composition of the steel (in wt%) is listed in Table 1. The steel samples are prepared in the size of $20 \times 10 \times 3$ mm, followed by grinding with SiC paper down to P600 grit to remove impurities and ensure uniform surface roughness across all samples. After grinding, the samples are thoroughly washed with deionized water and acetone. A total of 32 steel samples were prepared for the two experiments, with four samples per crucible: two for 600 h exposure and two for 1224 h. This arrangement maintained a minimum spacing of 10 mm between samples to ensure uniform exposure to the molten salt, also to avoid mutual influence on corrosion behavior. For each exposure time, one sample was used for weight gain and mass loss measurements, while the other was used for corrosion morphology analysis. The 400 ppm NO gas test is referred to as Test 1, and the 600 ppm NO gas test as Test 2, as shown in Table 2. The oxygen, and nitrogen gas flow rates are adjusted according to the required vol % of oxygen in each crucible.

The crucibles with salts were heated to 600°C and kept for 600 h or 1224 h. During the test, initial salt samples were drawn at

TABLE 1 | The nominal elemental composition in wt.% of the 310N austenitic steel.

Alloy	C	Cr	Ni	Mn	Si	P	S	N	Fe
310N	≤ 0.10	24.00–26.00	19.00–22.00	≤ 2.00	≤ 1.5	≤ 0.045	≤ 0.015	≤ 0.11	Balance

TABLE 2 | Test matrix depicting each crucible atmospheric condition and post-analysis techniques carried out for 600–1224 h exposures at 600°C in solar salt.

Crucible ID	NO gas concentration (ppm)	Oxygen (vol%)	Salt post analysis	Steel post analysis
Test1_O5	400	5	IC, Titration, MP-AES	Weight change, mass loss by descaling, SEM-EDX
Test1_O30	400	30		Weight change, mass loss by descaling
Test1_O55	400	55		Weight change, mass loss by descaling
Test1_O80	400	80		Weight change, mass loss by descaling, SEM-EDX
Test2_O15	600	15		Weight change, mass loss by descaling, FIB-EDX
Test2_O30	600	30		Weight change, mass loss by descaling
Test2_O45	600	45		Weight change, mass loss by descaling
Test2_O60	600	60		Weight change, mass loss by descaling, SEM-EDX

$t = 0$ h, once the salt temperature reached 600°C, and additional samples were collected at 600 h and 1224 h. After the 600 h and 1224 h corrosion tests, the gas flow was stopped and the crucibles were opened to extract the 600 h steel samples. After removal, the crucibles were sealed again and the gas flow was resumed. The same procedure was followed to extract the 1224 h steel samples. The following subchapter outlines the post-analysis of salt and steel samples.

2.3 | Post Analysis

2.3.1 | Salt Post Analysis

The molten salt samples collected from each crucible were analyzed for the following anions: nitrate, nitrite and chromate ions, and oxide ions.

Salt samples were analyzed using ion chromatography (IC) (Metrohm model 880 Basic IC plus, Germany) for nitrate, nitrite, and chromate ions. For ion chromatography, 125 mg of salt was dissolved in 500 mL of ultra-pure water and analyzed. A detailed description of the experiment and calibration is provided elsewhere [6].

Acid-base titration (Metrohm Titrando 800, Herisau, Switzerland) was performed to find the oxide ions concentrations in the salt. For titration, 500 mg of salt was dissolved in 160 mL of water and titrated with 0.01 M HCl (Titrisol standard solution). The exact concentration of HCl in the titration solution was determined by titer analysis using sodium carbonate (Merck, Germany, purity > 99.5%). The concentration of oxide ions measured through titration is generally depicted as O^{2-}, regardless of the specific oxide species present in the solar salt. The analytical techniques and statistical evaluation of the titration methods are detailed elsewhere [28].

2.3.2 | Steel Post Analysis

Out of the total four samples in each crucible, two steel samples were taken out after the 600 h and another two samples for the 1224 h corrosion test. Out of the two steel samples, one was used to calculate weight change and corrosion rate through descaling, and the other was analyzed using scanning electron Microscopy with energy dispersive X-ray spectroscopy (SEM-EDX) or focused ion beam with energy dispersive X-ray spectroscopy (FIB-EDX) to determine the corrosion layer thickness and morphology.

The steel samples were extracted after 600 and 1224 h. After the corrosion test the samples were cleaned with deionized water, dried overnight, and weighted to get the area specific weight change (mg/cm^2). The area specific weight change was calculated as per below Equation (3).

$$\Delta w = \frac{m_f - m_i}{S_0} \tag{3}$$

Where Δw is the weight change per unit area (mg/cm^2), m_f is the final sample weight after washing with deionized water following the corrosion test in (mg), m_i is the initial sample mass in (mg) and S_0 is the sample surface area in (cm^2) measured before the corrosion test. A positive value of Δw corresponds to a weight gain and a negative value to a mass loss.

The corrosion rate (μm/year) was calculated as per Equation (4), where m_d is the final mass of the sample after the descaling as described in ASTM G1(C7.4). The descaling process was repeated for 10 to 15 successive cycles until a steady mass loss was achieved. The mass loss per unit area was calculated according to Equation (4).

$$\Delta m = \frac{m_i - m_d}{S_0} \tag{4}$$

The corrosion rate per year was further calculated by linear extrapolation of 1224 h corrosion test as per Equation (5).

$$CR\left(\frac{\mu m}{y}\right) = \frac{87600 * \Delta m}{t * \rho} \tag{5}$$

Where Δm is the mass loss per unit area in mg/cm^2 calculated from Equation (4), t is time in hours of corrosion test and ρ is the density of steel (7.90 g/cm^3).

The surface and cross-sectional characterization of the corrosion/oxide layer products formed on the steel samples upon exposures in molten solar salt at 600°C at various N_2–O_2 atmospheres with 400 and 600 ppm NO gas for 600 and 1224 h, was analyzed using SEM-EDX (SEM—Tescan Vega3, Zeiss Crossbeam 350) and/or FIB-EDX (FEI-FIB Quanta 3D FEG), respectively. For the oxidation layer analysis by SEM-EDX, the following protocol is used. The steel samples from the 400 ppm NO experiments were mounted in epoxy resin, followed by grinding and polishing, and then analyzed using SEM-EDX. During the metallographic cross-sectioning, spallation of the oxide layer was observed, prompting careful examination. For the 600 ppm NO experiment, a different approach was used to avoid fracturing or removing the oxide layer. First, an Au-coating followed by an electrochemical deposition of Ni-coating were applied. Then, the samples were mounted in an epoxy resin for an appropriate grinding and polishing. Due to fragility and/or spallation nature of the oxidation layer, the FIB-EDX was used to accurately represent the structure of the oxidation layer without damaging it. In that case, as a common practice to protect the oxidation layer, depositing an electron-beam assisted Pt-coating before FIB-milling was carried out. Upon completion of the FIB-milling, the oxidation layer was analyzed by EDX coupled with the FIB-machine. The images obtained from these analyses were further processed using ImageJ software to measure the corrosion layer thickness. Measurements were taken at 10 to 15 different locations, and the standard deviation was calculated and presented in the results section.

3 | Results

3.1 | Salt Analysis

This section analyzes the changes in salt chemistry in terms of nitrate, nitrite, chromate, and oxide ions. Subsection 3.1.1 discusses the case with 400 ppm NO gas, followed by Subsection 3.1.2, which covers the results for 600 ppm NO gas.

3.1.1 | Salt Chemistry in 400 ppm NO

To analyze the impact of the oxygen vol% on the salt chemistry, the results from the first test conducted at 400 ppm NO with

oxygen concentration ranging from 5 vol% to 80 vol% are presented. This includes *nitrate, nitrite, and chromate ion* concentrations measured by IC, followed by *oxide ion* concentration measured by titration.

First, the results for nitrate ions are presented, followed by oxide ions and, finally, chromate ions, all measured after 1224 h. As shown in Figure 1, the *nitrate ion* concentration is found to be 81.1, 91.8, 93.8, and 95.1 mol% at 5, 30, 55, and 80 vol% oxygen respectively. Results show a steady increase in nitrate ion concentration with oxygen vol%. Additionally, based on the thermodynamic parameters reported by Nissen and Meeker [4, 32] ($\Delta H = 95\ \text{kJ mol}^{-1}$, $\Delta S = 84\ \text{J mol}^{-1}\ \text{K}^{-1}$), the standard Gibbs energy at 600°C (873 K) is obtained as $\Delta G° = 21.7\ \text{kJ mol}^{-1}$. The corresponding equilibrium constant using $K = \exp(-\Delta G°/RT)$, is $K = 0.0505\ \text{atm}^{-1/2}$.

For the nitrate–nitrite equilibrium given by Equation 1, the equilibrium constant can be expressed as

$$K = [NO_2^-](P_{O_2})^{\frac{1}{2}}/[NO_3^-] \tag{6}$$

$[NO_3^-]$ and $[NO_2^-]$ represent the concentration of nitrate and nitrite ions respectively and $(P_{O2})^{1/2}$ represents the square root of the oxygen partial pressure. Using this relationship and the thermodynamic data, the calculated equilibrium nitrate concentrations are 81.6 mol%, 91.6 mol%, 93.6 mol%, and 94.7 mol% at 5, 30, 55, and 80 vol% oxygen, respectively, at 600°C. The calculated nitrate concentration with increasing O_2 vol% aligns well with Equation 1, demonstrating that an increase in oxygen vol% shifts the equilibrium toward the left-hand side, producing more nitrate and also these values closely align with the experimental nitrate and nitrite concentration obtained in this study.

The *oxide ions* after 1224 h are found to be 0.121 mol%, 0.032 mol%, 0.024 mol%, and 0.015 mol% for 5, 30, 55, and 80 vol % oxygen, respectively. These values are below the defined critical corrosion limit of 0.25 mol% at 600°C for stainless steel. Above this limit, corrosion can accelerate, leading to increased material degradation and the consumption of these ions due to the corrosion process [26]. Additionally, the measured oxide concentration in this study is significantly lower as compared to a normal air atmosphere without NO, which shows up to 0.4 mol% oxide ions at 600°C after 1000 h [15]. This difference may be attributed to the presence of NO in the atmosphere, which could shift the equilibrium in the reaction shown in Equation 2 to the left-hand side, suppressing the oxide ion formation.

Chromate ions measured after 1224 h were found to be 0.008, 0.009, 0.006, and 0.012 mol% at 5, 30, 55, and 80 vol% oxygen, respectively. These values are above the detection limit (LD) of chromate in the IC measurements, which is 5 mmol% (0.005 mol%) [14]. These ions are not typically detected in blank solar salt experiments where no steel is present. However, they were observed in experiments involving steel, suggesting that the presence of steel contributes to chromate formation. Additionally, the chromate concentration does not exhibit a clear trend with increasing oxygen gas concentration. However, in a typical experiment conducted under an air atmosphere (20 vol% oxygen) at 600°C for 1000 h, chromate concentrations have been reported to reach up to 0.05 mol% [23], which is approximately five times higher than the values observed in the current study. A detailed discussion of this phenomenon is provided after discussing the corrosion aspect in the Section 4 Discussion.

3.1.2 | *Salt Chemistry in 600 ppm NO*

The *nitrate anion* concentration measured after 1224 h corrosion test in 600 ppm NO with varying oxygen vol% from each crucible is shown in Figure 2. Nitrate concentration increases from 88.4 mol% to 91.2 mol%, 93.5 mol%, and remains at 93.5 mol% as the oxygen gas concentration rises from 15 to 30, 45, and 60 vol%, respectively. As explained in earlier subsection 3.1.1, the nitrate concentration is strongly dependent on oxygen vol% and temperature. Additionally, thermodynamic calculations based on Nissen and Meekers data predict increasing nitrate concentrations of 88.5, 91.6, 93.0, and 93.9 mol% at 15, 30, 45, and 60 vol% oxygen, respectively at 600°C [4]. The measured concentrations align closely with

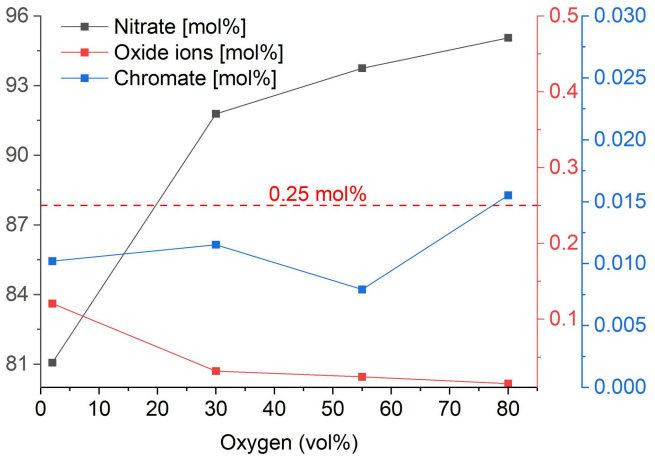

FIGURE 1 | Variation in nitrate, chromate, and oxide ion concentrations at 600°C after 1224 h exposure with 400 ppm NO and varying oxygen vol% (0.25 mol% dash line indicating oxide ion critical corrosion limit [26]). [Color figure can be viewed at wileyonlinelibrary.com]

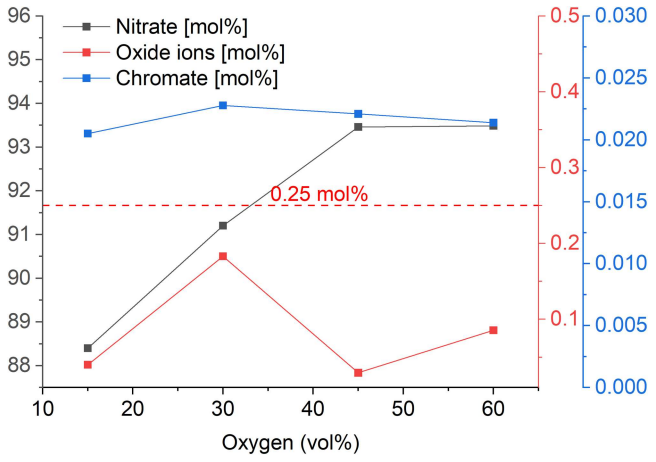

FIGURE 2 | Variation in nitrate, chromate, and oxide ion concentrations at 600°C after 1224 h exposure with 600 ppm NO and varying oxygen vol% (0.25 mol% dash line indicating oxide ion critical limit [26]). [Color figure can be viewed at wileyonlinelibrary.com]

these predictions, confirming the dependence of nitrate concentration on oxygen vol%.

The measured *oxide ion* concentrations were 0.04, 0.18, 0.03, and 0.09 mol% for 15, 30, 45, and 60 vol% oxygen, respectively. These values are below the defined critical corrosion limit at 600°C for stainless steel as explained in the earlier section. Similar to the previously observed oxide ion concentration, the concentration of oxide ions does not show a clear trend with increasing oxygen vol%. Moreover, similar to the 400 ppm NO experiment the oxide ion concentration in 600 ppm NO is also suppressed compared to normal synthetic air atmosphere.

The *chromate ion* was detected in all four crucibles, attributed to the dissolution of chromium from the 310N stainless steel sample in the salt melt at 0.021, 0.023, 0.022, and 0.021 mol% for 15, 30, 45, and 60 vol% oxygen, respectively. The chromate concentration shows only a minor variation with oxygen vol%. These values are also very low compared to earlier detected chromate levels after 1000 h of experiment in synthetic air at 600°C [23]. The detailed mechanistic discussion and reaction equations are retained in Section 4.

3.2 | Corrosion

3.2.1 | *Influence of Oxygen Concentration in 400 ppm NO on Steel Corrosion*

The following subsection will present the results for weight gain, corrosion rate through descaling, and SEM-EDX analysis for the Test 1- 310 N SS samples with 400 ppm NO. First the weight gain results are discussed followed by the corrosion rate from descaling, and finally the SEM-EDX results are discussed.

The *weight gain* results are shown in Figure 3a. After 600 h, the weight gains were 0.74, 0.70, 0.60, and 0.60 mg/cm^2 at 5, 30, 55, and 80 vol% oxygen, respectively. After 1224 h, the weight gains were 0.74, 0.70, 0.60, and 0.55 mg/cm^2 at 5, 30, 55, and 80 vol% oxygen, respectively. The samples exposed to 5 and 80 vol% oxygen show no significant weight changes at either 600 or 1224 h. Additionally, the values corresponding to each oxygen vol% remain consistent between the 600 and 1224 h exposures, indicating minimal variation with time. Overall, all the steel samples exhibited comparable weight gains with varying oxygen vol% or increasing time after the corrosion test, with no significant differences between them. The increase in weight after the corrosion product is attributed to the formation of corrosion products on the surface of the steel. However, similar weight gain does not necessarily indicate a similar amount of corrosion product formation, as detachment or spallation of corrosion products during the test can lead to variations in the measured values.

To find out how much base metal is consumed by the corrosion process the corrosion layer is removed by descaling and the *corrosion rates* are calculated based on Equation 5. As shown in Figure 3b, the corrosion rate for 5, 30, 55, and 80 vol% oxygen shows 40.8, 46.9, 43.3, 51.1 μm/year after 600 h and 22.8, 22.4, 23.7, 22.7 μm/year after 1224 h. Although the corrosion rate shows a slight increase with increasing oxygen volume percentage after 600 h, it eventually stabilizes at a similar level after long-term exposure of 1224 h. Overall, the corrosion rate decreased over time, which may suggest a typical parabolic behavior. Additionally, the change in oxygen vol% did not affect the corrosion rate beyond 1224 h, indicating that variations in oxygen vol% from 5 to 80 vol% does not have a significant impact on corrosion under 400 ppm NO gas in long term. To investigate the cause of this change, surface analysis was performed using SEM, followed by cross-sectional analysis of the corrosion layer on the steel.

First, *SEM surface analysis* was performed on the corroded samples that had been previously cleaned with deionized water. This was followed by cross-sectional analysis. The surface SEM images at 1224 h is shown in Figure 4. The analysis reveals that the morphology of the corrosion layer on the surface shows a distinct pattern as shown in Figure 4a, with 5 vol% oxygen samples showing densely packed needle-like structures with a flaky appearance, while as shown in Figure 4b,c, the surfaces at 30 and 55 vol% oxygen show mixed particle sizes with larger, well-faceted crystals. As shown in Figure 4d, the surface at 80 vol% oxygen exhibits a crystalline structure with densely packed, finer crystals. Overall, the surface analysis reveals different crystalline structure on the corrosion layer at 5 vol% to 80 vol% oxygen. To investigate the subsurface characteristics, cross-sectional analysis was conducted on both the samples tested for 600 and 1224 h.

The *SEM-EDX cross-sectional analysis* of the sample exposed to 5 vol% oxygen at 600 (Figure 5) and 1224 h (Figure 6) is presented. First, the corrosion layer morphology is discussed, followed by elemental analysis and a comparison of corrosion layer thickness.

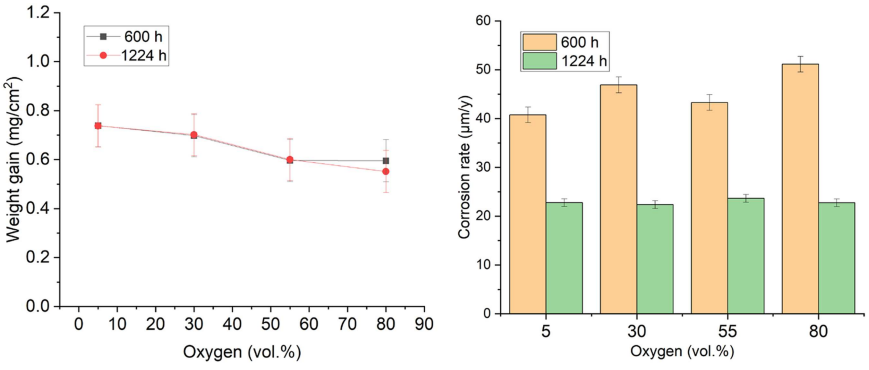

FIGURE 3 | (a) Weight gain and (b) corrosion rate by descaling of 310N SS after 600 and 1224 h corrosion in solar salt at 600°C under 400 ppm NO-containing atmosphere with varying oxygen vol%. [Color figure can be viewed at wileyonlinelibrary.com]

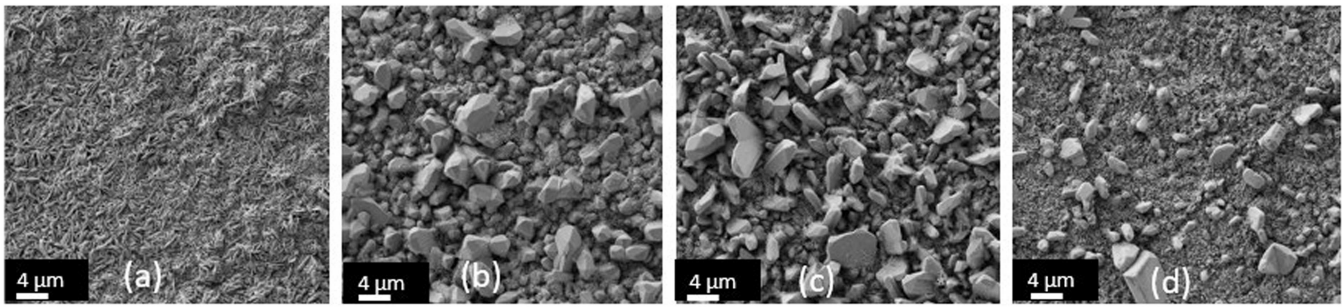

FIGURE 4 | Surface morphology of 310N SS after 1224 h corrosion test in solar salt at 600°C, under 400 ppm NO with (a) 5 vol% oxygen (b) 30 vol % oxygen (c) 55 vol% oxygen (d) 80 vol% oxygen.

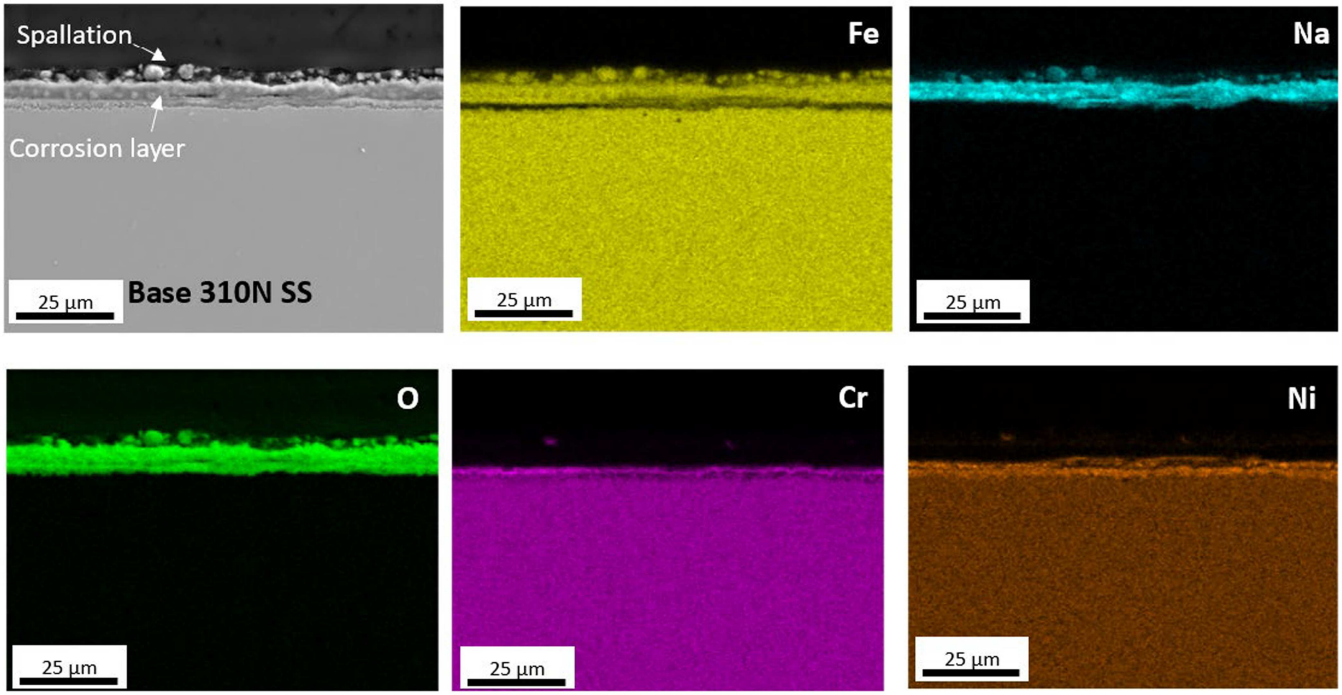

FIGURE 5 | SEM Cross-Section of 310N steel with respective EDX elemental maps obtained after 600 h of corrosion in solar salt at 600°C under 400 ppm NO with 5 vol% oxygen atmosphere. [Color figure can be viewed at wileyonlinelibrary.com]

As shown in Figure 5, the SEM *cross-section* of steel samples exposed to 5 vol% oxygen at 600 h reveals a dense corrosion layer with spallation occurring at the top of the layer. Similarly, as shown in Figure 6, the corrosion layer of 5 vol% oxygen at 1224 h is dense, with spalled particles visible on the surface. Spalled particles were observed only on samples prepared with epoxy resin (e.g., at 400 ppm NO). In contrast, no spallation was observed on samples prepared with a Ni-coating (e.g., at 600 ppm NO), which is consistent with its purpose of preventing metallographic preparation-induced oxide detachment. Therefore, the observed flaking is most likely an artifact introduced during metallographic preparation rather than oxide detachment or corrosion-induced spallation.

Based on the *elemental distribution,* the top corrosion layer are found to be sodium, iron, and oxygen, indicating the formation of sodium iron oxide layer. Beneath this layer, iron and oxygen are present, possibly due to the formation of an iron oxide corrosion layer. Below this, chromium and oxygen are observed, indicating the formation of a chromium oxide layer. Further beneath, a chromium-depleted zone or a nickel-enriched zone is visible. This type of layered corrosion is commonly observed in stainless steel samples exposed to solar salt. The top corrosion layer, a well-known corrosion product of high-temperature exposure in solar salt, forms on the surface and suggests the formation of $NaFeO_2$ or a related compound at 600°C [33, 34]. Just beneath this layer, hematite or magnetite iron oxides form, and further below is the chromium oxide layer, which is known to act as a protective barrier against corrosion [35]. SEM corrosion section layer thickness measured using ImageJ software showed values of 6.14 ± 0.72 µm at 600 h and 6.16 ± 0.78 µm at 1224 h (mean $\pm$ standard deviation, $n = 10$) for 5 vol% oxygen, which are comparable to each other. The similar corrosion layer thickness may be attributed to spallation, as illustrated in Figure 6.

The SEM cross-sectional analysis of samples exposed to 80 vol% oxygen for 1224 h is presented in Figure 7. The sample exposed to 80 vol% oxygen for 600 h did not reveal any significant new information and is therefore included in Appendix A. A multilayered,

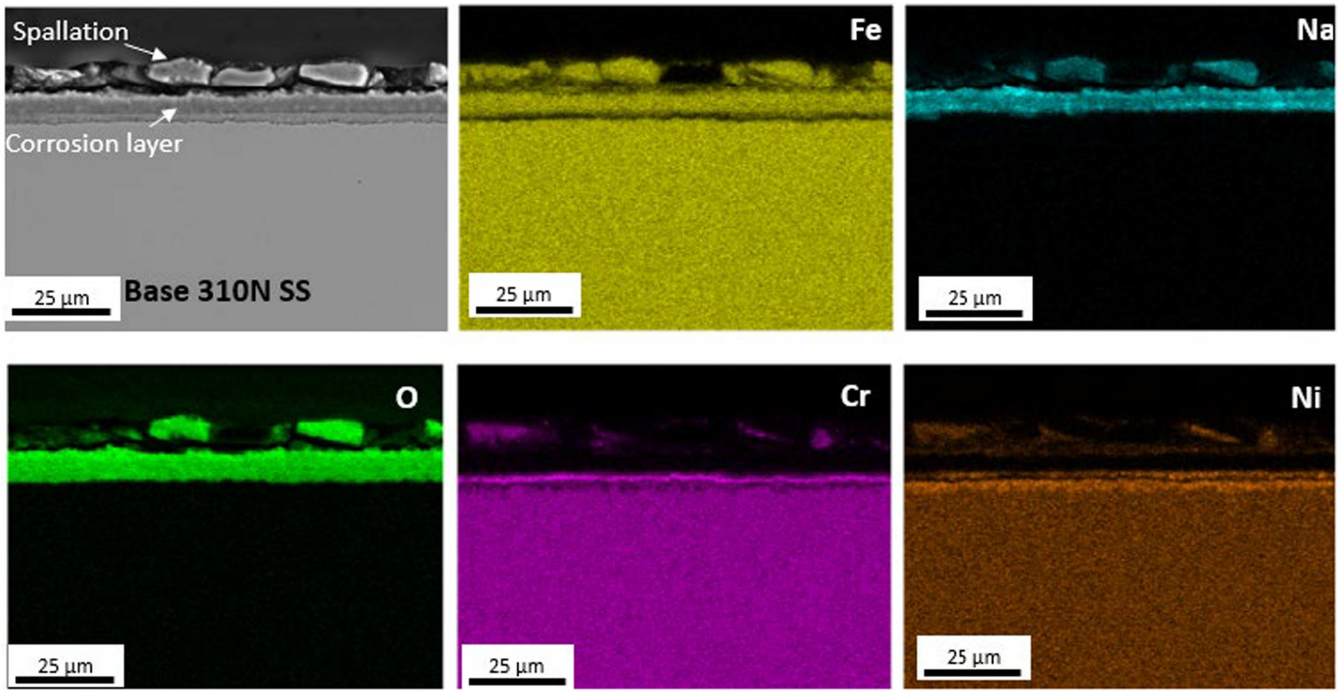

FIGURE 6 | SEM Cross-Section of 310N steel with respective EDX elemental maps obtained after 1224 h of corrosion in solar salt at 600°C under 400 ppm NO with 5 vol% oxygen atmosphere. [Color figure can be viewed at wileyonlinelibrary.com]

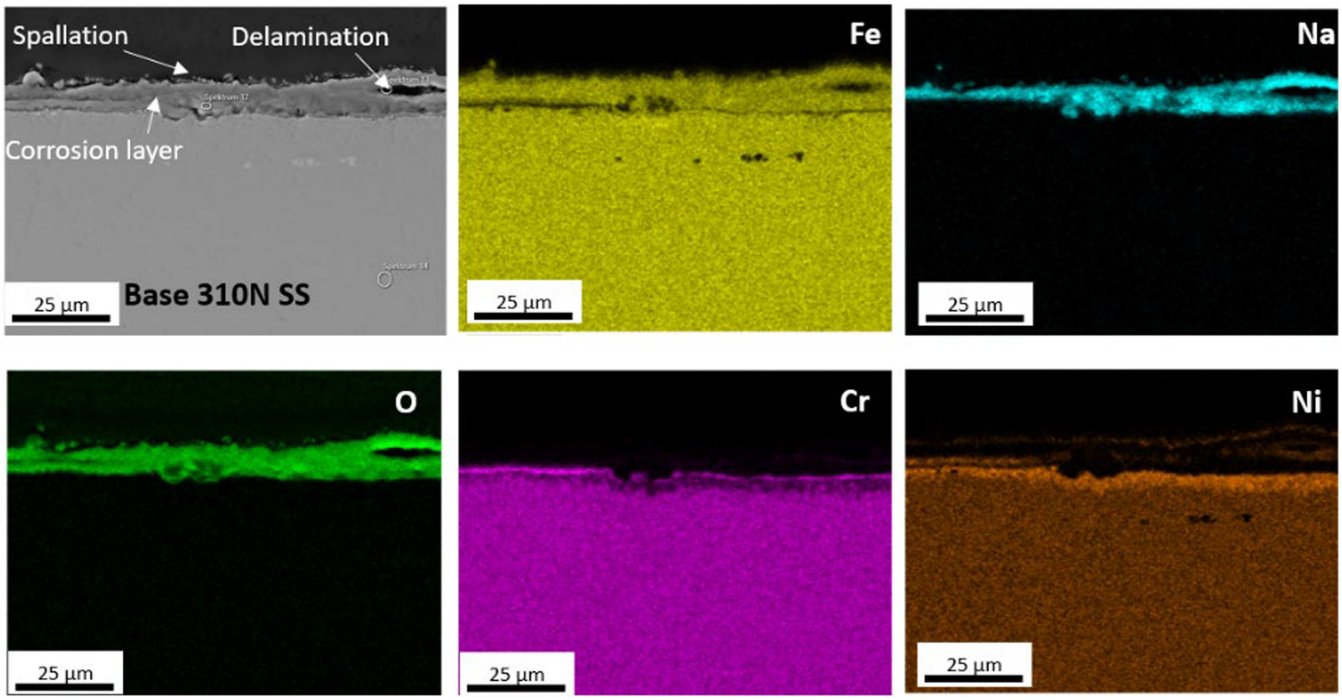

FIGURE 7 | SEM Cross-Section of 310N steel with respective EDX elemental maps obtained after 1224 h of corrosion in solar salt at 600°C under 400 ppm NO with 80 vol% oxygen atmosphere. [Color figure can be viewed at wileyonlinelibrary.com]

dense corrosion structure, similar to that observed at 5 vol% oxygen, is evident. For 80 vol% oxygen at 600 h, the corrosion layer thickness was found to be 5.93 ± 0.57 µm (mean ± standard deviation), indicating a comparable corrosion layer thickness to that observed at 5 vol% oxygen at 600 h. For 1224 h the corrosion layer thickness increases to 7.55 ± 1.35 µm (mean ± standard deviation) which is also close to the 5 vol% oxygen case at 1224 h. Overall, the corrosion layer thickness remained relatively steady from 600 h to 1224 h, indicating limited growth or spallation during extended exposure. Moreover, the corrosion layer thickness at 1224 h is similar for both 5 vol% and 80 vol% oxygen exposures. The corrosion layer thickness also aligns with the corrosion rate by descaling, since the corrosion rate is comparable for 5 vol% and 80 vol% oxygen concentration. The presence of delamination in the

corrosion layer of the SEM cross-section, as observed in Figure 7 after 1224 h of exposure, suggests that corrosion layer thickness alone may not reliably indicate the extent of degradation. However, the similar corrosion rates determined by descaling for both 5 and 80 vol% oxygen after 1224 h imply comparable corrosion layer thicknesses in both cases. Additionally, it is important to note that the distinct surface morphology observed in Figure 4 is limited to the surface layer, with no measurable impact on the density or integrity of the underlying corrosion layer. This phenomenon, while notable, will not be discussed in detail here as it does not affect the primary conclusions of this study. To fully understand the corrosion damage, it is important to consider the weight gain after corrosion, the calculated corrosion rates, and cross-sectional examinations. These aspects are covered in detail in Section 4.

3.2.2 | *Influence of Oxygen Concentration in 600 ppm NO on Steel Corrosion*

As shown in Figure 8a, the *weight gain* after 600 h for 15, 30, 45, and 60 vol% oxygen is 0.46, 0.90, 0.83, and 0.90 mg/cm^2, respectively. However, after 1224 h, the weight gain measuring 0.77, 0.95, 0.79, and 1.02 mg/cm^2, respectively. The weight gain values remain similar across all oxygen levels after 1224 h. This indicates a weight gain across all samples, resulting from the corrosion process, and suggests the formation of corrosion products on the steel surface, similar to the 400 ppm NO.

The *corrosion rate* determined by descaling for 15, 30, 45, and 60 vol % oxygen shows 26.6, 43.3, 44.2, 52.8 μm/year after 600 h and 30.4, 31.9, 26.9, 33.3 μm/year after 1224 h. Similar to the earlier exposure test with 400 ppm, the 600 ppm case also shows a similar trend. The corrosion rate initially increases slightly at 600 h with increasing oxygen gas concentration but eventually stabilizes at 1224 h. This indicates that, in the long term, the corrosion rate remains unaffected by increased oxygen gas concentration. Interestingly, compared to other oxygen concentrations, the corrosion rate at 15 vol% oxygen is lower after 600 h but stabilizes at 30.4 μm/year after 1224 h. This suggests that while the initial corrosion rate is lower at 15 vol% oxygen compared to higher oxygen gas concentrations, it eventually reaches a similar rate over extended exposure.

To understand the reason for this change, *FIB cut* of the corrosion layer followed by EDX analysis was performed on samples exposed to 15 vol% oxygen at 600 h (Figure 9) and 1224 h (Figure 10). The variation in corrosion layer thickness and morphology for the two oxygen concentrations 15 vol% and 60 vol% is discussed below in detail.

FIB cross-sectional images for 15 vol% O_2 after 600 and 1224 h are presented in Figures 9 and 10, highlighting the layered corrosion morphology. Cross-sectional *SEM-EDX images* for 60 vol% O_2, showcasing elemental distribution and corrosion layer structure, are available in Appendices A.2 and A.3. The corrosion layer in Figure 9 and Figure 10 shows a dense multilayered corrosion layer structure, which is similar to the 400 ppm NO experiment. The outermost layer is enriched with sodium, iron, and oxygen, indicating the formation of sodium iron oxide, a commonly observed outer corrosion product in nitrate melts. Below this layer, a chromium- and oxygen-rich region indicates the formation of chromium oxide, with noticeable chromium depletion beneath it and a corresponding enrichment of nickel.

In contrast to the 400 ppm NO experiment, no spallation was observed in the samples prepared with a Ni coating. The improved preparation likely preserved the surface integrity and avoided artifacts during analysis. The corrosion layer thicknesses determined by cross-sectional analysis for 15 vol% oxygen at 600 ppm NO at 600 and 1224 h were found to be 4.63 ± 0.51 μm and 11.11 ± 1.39 μm, respectively, correlating with mass losses of 1.44 mg/cm^2 and 3.36 mg/cm^2, as calculated using Equation 4. Moreover, the corrosion layer thickness measured for 60 vol% oxygen at 600 and 1224 h is found to be 4.72 ± 1.25 μm and 9.59 ± 1.78 μm respectively indicating corrosion layer growth after 600 h. Furthermore, the corrosion layer thickness slightly increases from 600 to 1224 h, indicating slow but continuous growth over time. A detailed analysis of weight gain, corrosion rate, and cross-sectional morphology for both 400 ppm and 600 ppm NO exposures are presented in Discussion Section 4.

4 | Discussion

The influence of varying *O_2 and NO gas* concentrations on the formation of nitrate, nitrite, oxide, and *chromate ions* under different atmospheric conditions is initially examined. This is followed by *steel corrosion* results. Finally, the combined effects of gas atmosphere on salt chemistry and their consequent implications for corrosion behavior are systematically discussed.

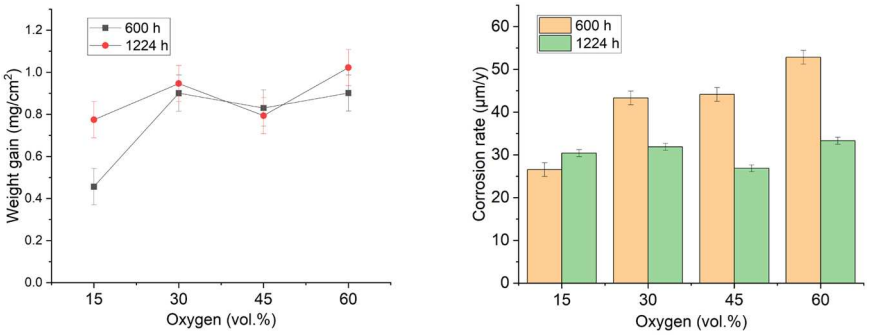

FIGURE 8 | (a) Weight gain and (b) corrosion rate by descaling of 310N SS after 600 and 1224 h corrosion in solar salt at 600°C under 600 ppm NO gas containing atmosphere with varying oxygen vol%. [Color figure can be viewed at wileyonlinelibrary.com]

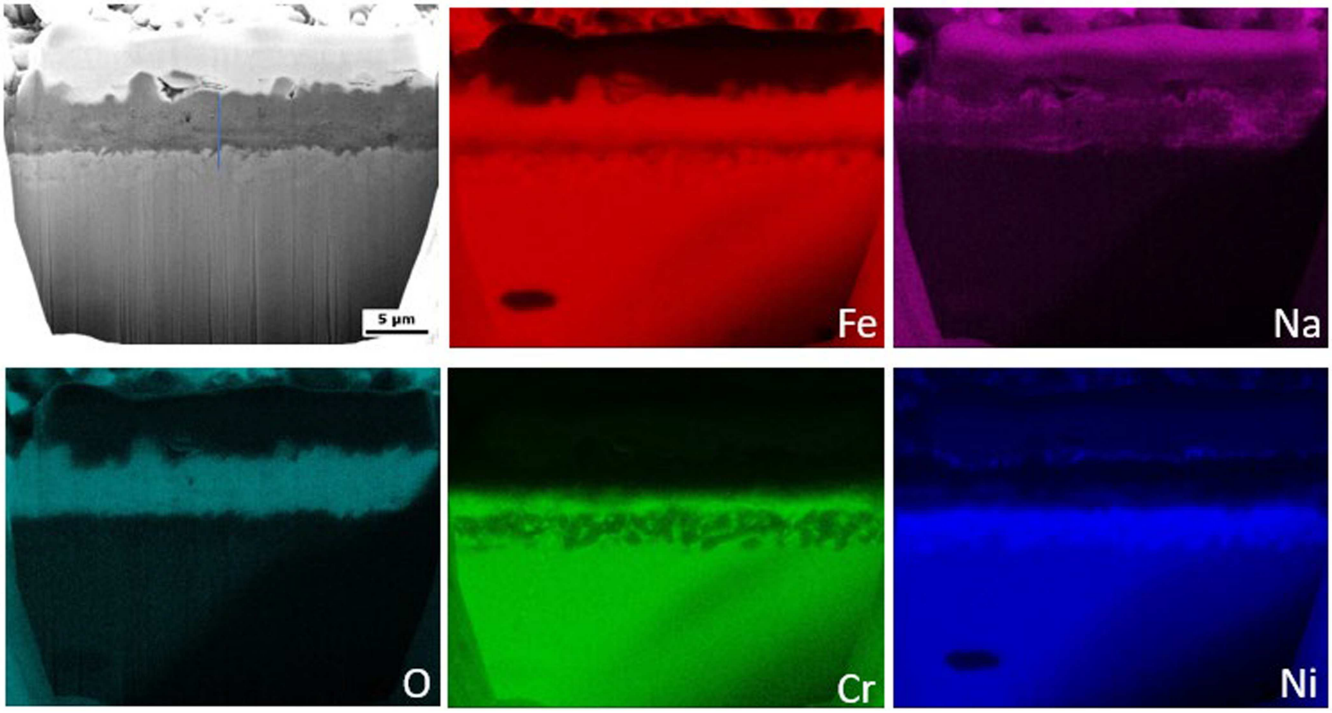

FIGURE 9 | Cross-Section by FIB-cut (top left) and the respective EDX element maps of SS310N stainless steel after 600 h of exposure in solar salt under 600 ppm NO with 15 vol% O_2 gas atmosphere at 600°C. [Color figure can be viewed at wileyonlinelibrary.com]

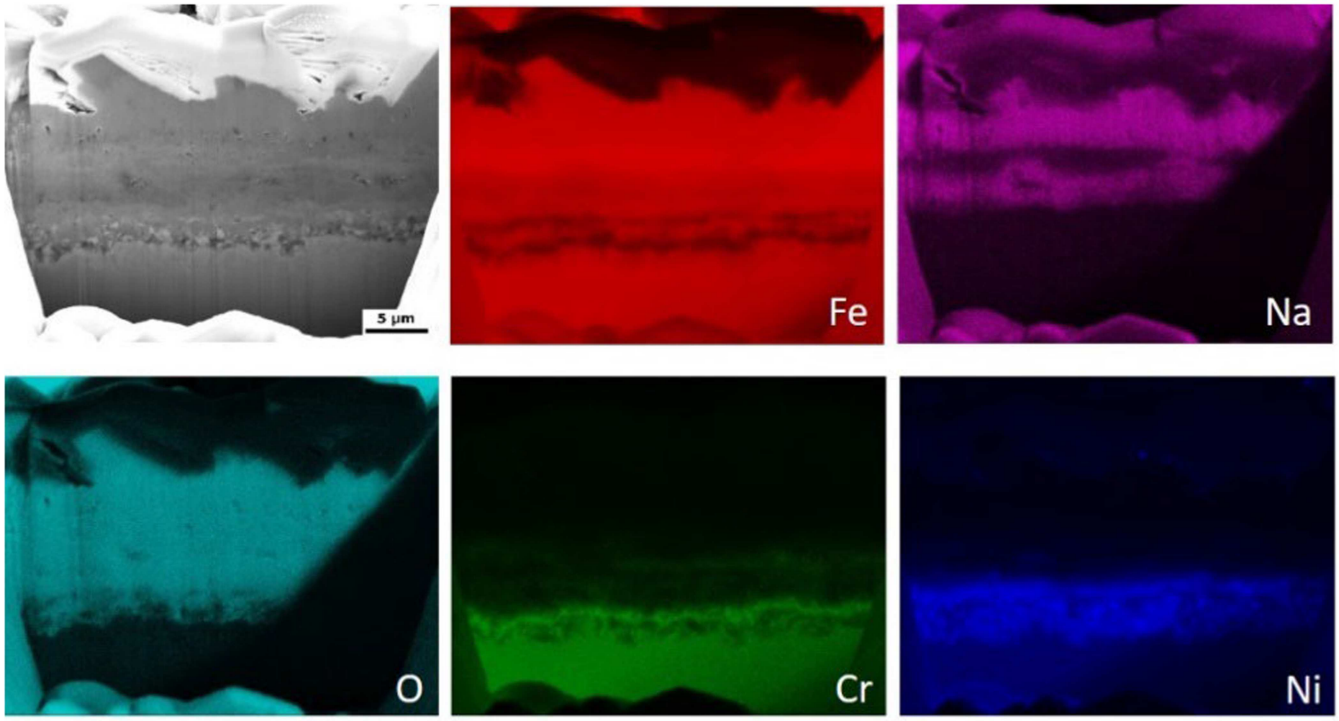

FIGURE 10 | Cross-Section by FIB-cut (top left) and the respective EDX element maps of SS310N stainless steel after 1224 h of exposure in solar salt under 600 ppm NO with 15 vol% O_2 gas atmosphere at 600°C. [Color figure can be viewed at wileyonlinelibrary.com]

The *salt chemistry analysis* conducted in this study reveals that the decomposition of nitrate ions decreases with increasing *oxygen vol%*. At the minimum oxygen vol% concentration of 5 vol% used in this experiment, the nitrate concentration was measured at 81.1 mol%, which is notably higher compared to 0 vol% O_2 (pure nitrogen). Under 0 vol% O_2 conditions, the nitrite ion concentration increased significantly, reaching up to 50 mol% after 1250 h of exposure at 560°C in solar salt [14]. This is attributed to the effective suppression of the initial decomposition step by oxygen gas as shown in Equation 1,

where nitrate ions typically convert to nitrite ions. Furthermore, the suppression of nitrite ion formation also contributes to a corresponding suppression in oxide ion formation, indicating a strong interdependence among these ionic species in molten salt chemistry [32].

Moreover, the addition of *NO gas* to an oxygen containing atmosphere reduces the oxide ion concentration. For both 400 ppm and 600 ppm NO, the oxide ion concentration is stabilized at significantly lower levels in contrast to conditions with 20 vol% O_2 alone. For example, all oxygen concentrations examined in this work and both NO levels of 400 and 600 ppm NO, the oxide level is around 0.2 mol% well below previously identified corrosion limit of 0.25 mol% oxides related to the anions mol% at 600°C. In contrast, experiments without NO report oxide ion concentrations exceeding 0.4 mol% at 600°C after 1000 h [23]. As reported by Steinbrecher et al. [31], the addition of NO alone is insufficient to stabilize oxide ion formation. Their study indicates that a minimum threshold of 5 vol % O_2 is required to suppress excessive nitrite accumulation, while at least 200 ppm NO is necessary to effectively limit the formation of oxide ions. These conditions define the lower gas boundary conditions for maintaining thermodynamic stability in solar salt at 600°C. This is further supported by Kunkel et al. [36], who demonstrated that during stabilization experiments of solar salt at 620°C in a semi-closed system, the concentration of NO_x ($NO + NO_2$) gradually stabilized to approximately 350 ppm over time. The results obtained from these experiments, along with supporting literature, indicate that the minimum of 5 vol% of oxygen and 200 ppm NO_x gas is sufficient to prevent increasing salt decomposition into nitrite and oxide ions over time. Overall, the combination of 5 vol% oxygen and 400 ppm NO employed in this study appears sufficient to stabilize salt decomposition, as evidenced by the nitrite and oxide ion concentrations observed in the salt chemistry results.

The detection of *chromate* in the salt confirms the dissolution of corrosion products (in particular, the Cr-rich oxides) in salt melt, also the SEM-EDX cross-sectional analyses consistently revealed chromium-rich oxide formation in the corrosion product. The formed chromium oxide corrosion layer can dissolve in solar salt as chromate in the presence of oxide ions or nitrate ions. The formation of chromate is explained by two proposed mechanisms, as shown in Equations 7 and 8 below [14, 37–40]. Given that oxide ions are suppressed to a low level in this experiment, it is likely that chromate formation predominantly occurs via Reaction Equation 8. This is further supported by Meißer et al. [41], who postulated that nitrate ions can oxidize iron, nickel, and chromium at 600°C during the initial stages of corrosion, particularly when nitrite and oxide ion formation is limited. Moreover, chromate formation is found to be higher in an air atmosphere at 600°C after 1000 h [23], compared to an oxygen and NO-containing atmosphere where NO suppresses oxide ion formation. This suggests that Reaction 7 may proceed faster in the presence of oxide ions, leading to increased chromium oxide layer dissolution from steels and chromate formation in the salt. Additionally, the density of the corrosion layer formed above the chromium oxide layer can also reduce the dissolution of chromium into the salt [22]. It is important to note that the nitrate/nitrite molten-salt mixture is moderately oxidizing in nature; therefore, the reduction of the formed chromate back to Cr_2O_3 is unlikely under the experimental conditions applied in this study.

$$Cr_2O_3 + 2O^{2-} + \frac{3}{2}O_2 \quad \rightleftarrows \quad 2CrO_4^{2-} \tag{7}$$

$$Cr_2O_3 + 5NO_3^- \quad \rightleftarrows \quad 2CrO_4^{2-} + NO_2^- + 4NO_2 \tag{8}$$

The changes in salt chemistry directly influence the *corrosion behavior of steel*, as reflected in weight gain, corrosion rates, and SEM observations. These findings are further correlated with salt chemistry variations in the following discussion.

The *corrosion analysis* of the steel samples reveals that the *weight gain* remains relatively stable across different oxygen concentrations (5–80 vol%) at both 600 h and 1224 h for 400 and 600 ppm NO exposure. The minimal difference observed over time suggests the establishment of a protective mechanism. This behavior can be attributed to either: (1) the formation of a passivation layer that effectively controls the diffusion of corrosive species into the metal matrix, or (2) a dynamic equilibrium between oxide layer formation and metal loss through spallation or dissolution. Both mechanisms contribute to limiting further weight gain despite the presence of oxygen. Interestingly, the *corrosion rate* determined by descaling decreases with time from 600 to 1224 h, indicating the formation of a protective and passive corrosion layer that limits further metal oxidation. However, at the short duration of 600 h for both 400 and 600 ppm NO, the corrosion rate increases with higher oxygen concentrations, suggesting that elevated oxygen levels enhance the initial oxidation process before the protective layer fully develops. This can be attributed to enhanced oxidation at the metal surface caused by increased nitrate concentrations in the salt resulting from higher oxygen concentration in the gas phase. As highlighted in literature [22, 42, 43], nitrate ions (NO_3^-) can directly oxidize the metal surface, contributing to the formation of corrosion products, as per Equations 9 and 10. This mechanism underscores the role of nitrate ions in the initial stages of corrosion.

$$Fe + NO_3^- \rightleftarrows FeO + NO_2^- \tag{9}$$

$$3Fe + 3NO_3^- \rightleftarrows Fe_3O_4 + NO_2^- + 2NO + O^{2-} \tag{10}$$

Elevated oxygen levels promote the formation of nitrate ions, which directly oxidize the metal surface, accelerating the initial corrosion rate. Over time, the buildup of corrosion product layers on the metal surface contributes to the development of a passive corrosion layer that stabilizes the corrosion rate (assuming suppressed oxide ions). The stabilization of weight gain and the reduction in corrosion rate over time support the presence of a protective oxide film that suppresses continued metal degradation or corrosion. However, these exposure times of 1224 h still represents the early-stage corrosion compared to the lifetime of a CSP plants (> 20 years). Over longer duration, the corrosion behaviour is expected to follow a parabolic kinetics, governed by diffusion through the already formed oxide layer which would slow down the corrosion and the overall corrosion rate further. Nevertheless, variations in gas composition, temperature, or mechanical stress can locally break the protective film and cause a transition to linear or even breakaway corrosion. Therefore, long-term studies are required to confirm the durability and stability of the protective layer under realistic operating conditions.

The *SEM-EDX analysis* shows that the corrosion layer formed on the steel has a typical corrosion layer structure with the

three distinct layers, which constitute of sodium iron oxide, iron oxide, chromium oxide, and the Ni-enrichment at the oxide-steel interface in the base metal. Compared to the steel samples exposed to air atmosphere at 600°C after 1000 h [23], the corrosion layer formed under NO gas containing conditions in this experiment is both denser and more stable, as evidenced by weight gain measurements and corrosion rate analysis. Furthermore, chromate ion in the salt is lower compared to that in an air atmosphere [23], indicating that the top sodium iron oxide or iron oxide layer above the chromium oxide acts as a diffusion barrier. This barrier slows chromium oxide dissolution, preserving the corrosion layers protective properties. The formation of denser and protective outer corrosion layer in the presence of NO gas is further supported by Bonk et al. [22]. Additionally, after 1224 h of exposure, the corrosion layer thickness does not exhibit any significant trend of increase or decrease with varying oxygen concentrations in the crucibles. This suggests that the growth of the corrosion layer may reach a steady state or be influenced by factors other than just oxygen concentration. The decrease in corrosion rate from 600 to 1224 h, coupled with consistent weight gain and stable corrosion layer thickness, highlights the development of a dense, passive layer that remains robust over time, regardless of oxygen availability. This behavior strongly suggests that in the presence of NO gas, the corrosion layer forms more gradually, contributing to effective passivation and enhanced long-term corrosion resistance.

Overall, the *gas atmosphere* significantly influences *salt chemistry*, which in turn affects the *corrosion behavior of steel*. A comparison of the results from this study with earlier research indicates that the absence of oxygen and exposure to a pure nitrogen atmosphere (0 vol% oxygen) lead to increased corrosion layer formation, accompanied by higher porosity and more defects in the corrosion layer. The absence of oxygen in the atmosphere promotes the formation of nitrite ions, which subsequently leads to increased generation of oxide ions and accelerated corrosion [14, 23]. In contrast, exposure to synthetic air with 20 vol% oxygen effectively suppresses the decomposition of nitrate ions, leading to the formation of a denser and more protective corrosion layer. At 600°C, for 1000 h of exposure in solar salt under air atmosphere, the corrosion layer exhibits reduced porosity and fewer cracks, indicating enhanced structural integrity compared to conditions with pure nitrogen atmosphere [23]. Furthermore, the addition of NO gas to the oxygen containing atmosphere in this experiment further suppresses the decomposition of nitrite ions into oxide ions, thereby enhancing the formation of a more stable passivation layer over time compared to nitrogen or air atmospheres. The major new contribution of the presented work is the variation of the oxygen gas concentration in the presence of NO gas. Increasing the oxygen vol% from 5 till 80 vol% in the presence of 400 or 600 ppm NO gas affects the nitrate ion concentration but does not significantly impact the long-term corrosion behavior of stainless steel at 600°C. Differences in corrosion rates are observed only during the initial stages of the process, while for longer exposure durations, the corrosion rates converge and show no significant dependence on oxygen gas concentration or nitrate concentration in the solar salt at 600°C.

In summary, salt chemistry is a critical factor that significantly influences the corrosion process. The stabilization of salt decomposition through the controlled presence of oxygen and NO gas promotes the formation of a passive corrosion layer. This protective layer effectively limits further oxidation and enhances the long-term durability of the stainless steel. It is also important to note that manipulating salt chemistry is a key strategy for reducing corrosion in solar salt, even at temperatures higher than 565°C. Effective control of salt decomposition can enhance passivation to corrosion, leading to improved stainless steel stability. Utilizing optimized and controlled atmospheres with O_2 and NO can extend the longevity of commercial solar salt applications at or above 565°C. Additionally, this approach may enable operation at higher temperatures, thereby improving the overall efficiency of these high-temperature plants.

5 | Conclusion

This study investigated the impact of varying oxygen concentrations in the presence of NO gas at 600°C over a duration of 1224 h. Both the salt chemistry and the corrosion behavior of the steel were analyzed to understand the influence of oxygen gas concentration on the underlying corrosion mechanisms. The salt chemistry was analyzed using ion chromatography (IC) to quantify nitrate, nitrite, and chromate ions, while titration was employed to determine the oxide ion concentration in solar salt. Steel corrosion was assessed through weight gain, corrosion rate by descaling measurements, and FIB cross-sectioning. Additionally, SEM-EDX analysis was performed to characterize the corrosion features on the steel surface. This led to the following conclusion:

- *Influence of gas atmosphere on salt chemistry:* Increasing the oxygen concentration in the cover gas effectively suppresses the decomposition of nitrate ions in solar salt, thereby also limiting the formation of both nitrite and oxide ions. While higher oxygen levels reduce the conversion of nitrate to nitrite, the presence of both 400 or 600 ppm NO gas further suppresses the subsequent formation of oxide ions, contributing to overall salt stability at 600°C till 1224 h. These experimental results reconfirm and reinforce findings previously reported in the literature.
- *Initial stage corrosion:* Previous studies have shown that the addition of NO can reduce corrosion rates by suppressing oxide ion formation. However, the impact of varying oxygen gas concentrations in the presence of NO has not been systematically addressed. This study fills that knowledge gap by demonstrating, for the first time, that at 600 h, increased oxygen concentrations lead to slightly higher initial corrosion rates for both 400 and 600 ppm NO conditions. This effect is likely due to enhanced nitrate ion concentration, which directly oxidizes the metal surface before a stable protective layer can fully develop.
- *Long term corrosion with increasing oxygen:* Despite varying oxygen concentrations (5–80 vol%) in the presence of 400 or 600 ppm NO gas, the long-term corrosion behavior measured by weight gain, corrosion rate, and corrosion layer thickness remained stable after 1224 h. This can be attributed to the formation of a dense, passive corrosion layer during the initial stage of corrosion, which subsequently suppresses further metal oxidation. Once passivation is established, the influence of oxygen gas concentration becomes minimal.

- *NO Gas impact on corrosion layer:* Corrosion layers formed in $O_2 + NO$ gas containing atmospheres are denser, more stable, and show fewer defects than those formed in pure nitrogen or air. SEM-EDX revealed dense, multilayered structures with a sodium-iron-oxygen rich outer layer, an iron-oxygen-rich intermediate layer, and a chromium-oxygen rich inner layer, indicating enhanced surface protection under NO exposure. Notably, variations in oxygen concentration above 5 vol% in the presence of 400 or 600 ppm NO do not significantly affect the chemistry and compactness of the formed corrosion layer, indicating that NO plays a dominant role in determining layer structure and stability under these conditions.
- *Oxygen and NO impact on salt chemistry and corrosion:* A combination of ≥ 5 vol% oxygen and ≥ 400 ppm NO effectively suppresses solar salt decomposition by stabilizing nitrate levels and limiting the formation of nitrite and oxide ions at 600°C. This control over salt chemistry by changing gas atmosphere also plays a key role in reducing long-term corrosion and maintaining stainless steel integrity.

Future research should investigate steel corrosion in gas atmospheres at 600°C without the presence of molten salt to isolate the effect of gas phase corrosion. Additionally, corrosion studies under NO gas-containing but oxygen-free atmospheres could further clarify the extent to which oxygen contributes to corrosion control and whether NO alone can play a stabilizing role. Moreover, long-term dynamic flow studies under controlled gas atmospheres are needed to better simulate real CSP-TES operating conditions and to gain deeper insights into corrosion mechanisms. Overall, findings from our studies offer strategies to mitigate corrosion in CSP-TES systems by optimizing the gas atmosphere above solar salt. Controlling the gas composition can enhance stainless steel component durability and potentially extend the operational temperature range of solar salt, improving thermal efficiency and system longevity.

Author Contributions

Sumit Kumar: funding acquisition, writing – review and editing, writing – original draft, visualization, validation, project administration, methodology, investigation, formal analysis, data curation, and conceptualization. **Srinivasan Swaminathan:** funding acquisition, conceptualization, writing – review and editing, writing – original draft, visualization, project administration, methodology, investigation, formal analysis, data curation. **Rene Hesse:** investigation, data curation. **Wenjin Ding:** writing – review and editing, supervision, formal analysis. **Thomas Bauer:** funding acquisition, writing – review and editing, validation, supervision, resources, project administration, and formal analysis.

Acknowledgments

The authors gratefully acknowledge the Deutsche Forschungsgemeinschaft (DFG, German Research Foundation) for support under project number 455432503 (MaDMoS). S. Kumar thanks M. Braun, R. Hoffmann, and A. Hanke for their assistance in the laboratories at DLR Stuttgart. Open Access funding enabled and organized by Projekt DEAL.

Conflicts of Interest

The authors declare no conflicts of interest.

Data Availability Statement

The data that support the findings of this study are available from the corresponding author upon reasonable request.

References

1. T. Bauer, C. Odenthal, and A. Bonk, "Molten Salt Storage for Power Generation," *Chemie Ingenieur Technik* 93 (2021): 534–546, https://doi.org/10.1002/cite.202000137.

2. M. Mehos, H. Price, R. Cable, et al., *Concentrating Solar Power Best Practices Study in National Renewable Energy Lab (NREL)* (Solar Dynamics, 2020), https://doi.org/10.2172/1665767.

3. B. D. Bond and P. W. M. Jacobs, "The Thermal Decomposition of Sodium Nitrate," *Journal of the Chemical Society A: Inorganic, Physical, Theoretical* 1966): 1265–1268, https://doi.org/10.1039/J19660001265.

4. D. A. Nissen and D. E. Meeker, "Nitrate/Nitrite Chemistry in Sodium Nitrate-Potassium Nitrate Melts," *Inorganic Chemistry* 22 (1983): 716–721, https://doi.org/10.1021/ic00147a004.

5. E. S. Freeman, "The Kinetics of the Thermal Decomposition of Potassium Nitrate and of the Reaction Between Potassium Nitrite and Oxygen," *Journal of the American Chemical Society* 79 (1957): 838–842, https://doi.org/10.1021/JA01561A015.

6. A. Bonk, C. Martin, M. Braun, and T. Bauer, "Material Investigations on the Thermal Stability of Solar Salt and Potential Filler Materials for Molten Salt Storage," *AIP Conference Proceedings* 1850 (2017): 080008, https://doi.org/10.1063/1.4984429.

7. A. Bonk, M. Braun, V. A. Sötz, and T. Bauer, "Solar Salt–Pushing an Old Material for Energy Storage to a New Limit," *Applied Energy* 262 (2020): 114535, https://doi.org/10.1016/j.apenergy.2020.114535.

8. J. Steinbrecher, A. Hanke, M. Braun, T. Bauer, and A. Bonk, "Stabilization of Solar Salt at 650° C–Thermodynamics and Practical Implications for Thermal Energy Storage Systems," *Solar Energy Materials and Solar Cells* 258 (2023): 112411, https://doi.org/10.1016/j.solmat.2023.112411.

9. R. I. Olivares, "The Thermal Stability of Molten Nitrite/Nitrates Salt for Solar Thermal Energy Storage in Different Atmospheres," *Solar Energy* 86 (2012): 2576–2583, https://doi.org/10.1016/j.solener.2012.05.025.

10. V. A. Sötz, A. Bonk, J. Steinbrecher, and T. Bauer, "Defined Purge Gas Composition Stabilizes Molten Nitrate Salt-Experimental Prove and Thermodynamic Calculations," *Solar Energy* 211 (2020): 453–462, https://doi.org/10.1016/j.solener.2020.09.041.

11. P. G. Zambonin and J. Jordan, "Redox Chemistry of the System O_2-O_2–O_{22}–O_2-in Fused Salts," *Journal of the American Chemical Society* 91 (1969): 2225–2228, https://doi.org/10.1021/ja01037a007.

12. P. G. Zambonin and J. Jordan, "Chemistry of Electron Transfer and Oxygen Transfer in Fused Salts," *Journal of the American Chemical Society* 89 (1967): 6365–6366, https://doi.org/10.1021/ja01000a075.

13. Á. G. Fernández and L. F. Cabeza, "Molten Salt Corrosion Mechanisms of Nitrate Based Thermal Energy Storage Materials for Concentrated Solar Power Plants: A Review," *Solar Energy Materials and Solar Cells* 194 (2019): 160–165, https://doi.org/10.1016/j.solmat.2019.02.012.

14. A. Bonk, M. Braun, A. Hanke, et al., "Influence of Different Atmospheres on Molten Salt Chemistry and Its Effect on Steel Corrosion," in *AIP Conference Proceedings* (AIP Publishing LLC, 2018), 0090003, https://doi.org/10.1063/1.5067097.

15. T. Tzvetkoff and J. Kolchakov, "Mechanism of Growth, Composition and Structure of Oxide Films Formed on Ferrous Alloys in Molten Salt Electrolytes—A Review," *Materials Chemistry and Physics* 87 (2004): 201–211, https://doi.org/10.1016/j.matchemphys.2004.05.039.

16. S. Bell, T. Steinberg, and G. Will, "Corrosion Mechanisms in Molten Salt Thermal Energy Storage for Concentrating Solar Power,"

Renewable and Sustainable Energy Reviews 114 (2019): 109328, https://doi.org/10.1016/j.rser.2019.109328.

17. M. C. Pavón-Moreno, A. Lopez-Paneque, J. M. Gallardo, A. Paul, E. Díaz-Gutierrez, and C. Prieto, "Critical Assessment of Migration Strategies for Corrosion in Molten Salts," *Materials* 18 (2025): 3804, https://doi.org/10.3390/ma18163804.

18. V. Encinas-Sánchez, E. Batuecas, A. Macías-García, C. Mayo, R. Díaz, and F. J. Pérez, "Corrosion Resistance of Protective Coatings Against Molten Nitrate Salts for Thermal Energy Storage and Their Environmental Impact in CSP Technology," *Solar Energy* 176 (2018): 688–697, https://doi.org/10.1016/j.solener.2018.10.083.

19. C. Oskay, T. M. Meißner, C. Dobler, B. Grégoire, and M. C. Galetz, "Scale Formation and Degradation of Diffusion Coatings Deposited on 9% Cr Steel in Molten Solar Salt," *Coatings* 9 (2019): 687, https://doi.org/10.3390/coatings9100687.

20. L. González-Fernández, Á. Serrano, E. Palomo, and Y. Grosu, "Nanoparticle-Based Anticorrosion Coatings for Molten Salts Applications," *Journal of Energy Storage* 58 (2023): 106374, https://doi.org/10.1016/j.est.2022.106374.

21. R. Xu, C. Zhang, L. Ma, G. Wang, Y. Wu, and Y. Lu, "Comparative Investigation on Dynamic Hot Corrosion Behavior of 347H in Quaternary Molten Salt and Its Nanofluids," *Solar Energy Materials and Solar Cells* 280 (2025): 113263, https://doi.org/10.1016/j.solmat.2024.113263.

22. A. Bonk, W. Ding, A. Hanke, et al., "Effect of Gas Management on Corrosion Resistance in Molten Solar Salt Up to 620°C: Corrosion of SS316-types and SS347," *Corrosion Science* 227 (2024): 111700, https://doi.org/10.1016/j.corsci.2023.111700.

23. S. Kumar, A. Hanke, A. Bonk, and T. Bauer, "Influence of Atmosphere and Austenitic Stainless Steel on the Solar Salt Corrosivity," *Heliyon* 10 (2024): e25966, https://doi.org/10.1016/j.heliyon.2024.e25966.

24. J. W. Slusser, J. B. Titcomb, M. T. Heffelfinger, and B. R. Dunbobbin, "Corrosion in Molten Nitrate-Nitrite Salts," *JOM* 37 (1985): 24–27, https://doi.org/10.1007/BF03259692.

25. K. Federsel, J. Wortmann, and M. Ladenberger, "High-Temperature and Corrosion Behavior of Nitrate Nitrite Molten Salt Mixtures Regarding Their Application in Concentrating Solar Power Plants," *Energy Procedia* 69 (2015): 618–625, https://doi.org/10.1016/j.egypro.2015.03.071.

26. S. Kumar, S. Swaminathan, R. Hesse, et al., "Understanding the Effect of Oxide Ions on Solar Salt Chemistry and Corrosion Mechanism of 316 L Stainless Steel at 600° C," *Corrosion Science* 249 (2025): 112849, https://doi.org/10.1016/j.corsci.2025.112849.

27. S. Swaminathan, S. Kumar, A. Kranzmann, R. Hesse, H. Goldbeck, and A. Fantin, "Corrosion Characteristics of 316L Stainless Steel in Oxide-Rich Molten Solar Salt at 600°C," *Solar Energy Materials and Solar Cells* 278 (2024): 113176, https://doi.org/10.1016/j.solmat.2024.113176.

28. J. Steinbrecher, A. Bonk, V. A. Sötz, and T. Bauer, "Investigation of Regeneration Mechanisms of Aged Solar Salt," *Materials* 14 (2021): 5664, https://doi.org/10.3390/ma14195664.

29. M. Mehos, C. Turchi, J. Vidal, et al., "Concentrating Solar Power Gen3 Demonstration Roadmap, National Renewable Energy Lab. (NREL) Golden, CO (United States)," 2017, https://doi.org/10.2172/1338899.

30. Producer or Source: Mannesmann DMV Stainless USA Inc, "DMV 310 N: Highly Creep-Resistant Austenitic Stainless Steel," *Alloy Digest* 58 (2009): SS-1027. https://doi.org/10.31399/asm.ad.ss1027.

31. J. Steinbrecher, M. Braun, T. Bauer, S. Kunkel, and A. Bonk, "Solar Salt above 600°C: Impact of Experimental Design on Thermodynamic Stability Results," *Energies* 16 (2023): 5241, https://doi.org/10.3390/en16145241.

32. V. A. Sötz, A. Bonk, J. Forstner, and T. Bauer, "Microkinetics of the Reaction NO3-⇌ NO2-+ 0.5 O2 in Molten Sodium Nitrate and Potassium Nitrate Salt," *Thermochimica Acta* 678 (2019): 178301, https://doi.org/10.1016/j.tca.2019.178301.

33. R. W. Bradshaw, "Thermal Convection Loop Study of the Corrosion of Incoloy 800 in Molten NaNO3-KNO3," *Corrosion* 43 (1987): 173–178, https://doi.org/10.5006/1.3583131.

34. A. Soleimani Dorcheh, R. N. Durham, and M. C. Galetz, "Corrosion Behavior of Stainless and Low-Chromium Steels and IN625 in Molten Nitrate Salts at 600 C," *Solar Energy Materials and Solar Cells* 144 (2016): 109–116, https://doi.org/10.1016/j.solmat.2015.08.011.

35. R. A. Rapp and N. Otsuka, "The Role of Chromium in the Hot Corrosion of Metals," *ECS Transactions* 16 (2009): 271–282, https://doi.org/10.1149/1.3159332.

36. S. Kunkel, F. Seeliger, A. Hanke, T. Bauer, and A. Bonk, "Demonstration of the Stabilization of Solar Salt at 620 C With a Semi-Closed Configuration in a 100 kg-Scale," *Heliyon* 9 (2023): e22363, https://doi.org/10.1016/j.heliyon.2023.e22363.

37. C. M. Kramer, W. H. Smyrl, and W. B. Estill, "Corrosion of Fe Alloys in NaNO3-KNO3-NaNO2 at 823 K," *Journal of Materials for Energy Systems* 1 (1980): 59–65, https://doi.org/10.1007/BF02833362.

38. A. Bonk, D. Rückle, S. Kaesche, M. Braun, and T. Bauer, "Impact of Solar Salt Aging on Corrosion of Martensitic and Austenitic Steel for Concentrating Solar Power Plants," *Solar Energy Materials and Solar Cells* 203 (2019): 110162, https://doi.org/10.1016/j.solmat.2019.110162.

39. R. A. Rapp, "The Hot Corrosion of Metals by Molten Salts," *ECS Proceedings Volumes*, no. 1981–10 (1981): 159–177, https://doi.org/10.1149/198110.0159PV.

40. B. J. Brough, D. H. Kerridge, and S. A. Tariq, "Molten Lithium-Potassium Nitrate Eutectic: The Reactions of Some Compounds of Chromium," *Inorganica Chimica Acta* 1 (1967): 267–270, https://doi.org/10.1016/S0020-1693(00)93183-9.

41. T. M. Meißner, C. Oskay, A. Bonk, et al., "Improving the Corrosion Resistance of Ferritic-Martensitic Steels at 600 C in Molten Solar Salt via Diffusion Coatings," *Solar Energy Materials and Solar Cells* 227 (2021): 111105, https://doi.org/10.1016/j.solmat.2021.111105.

42. A. G. Fernández, A. Rey, I. Lasanta, S. Mato, M. P. Brady, and F. J. Pérez, "Corrosion of Alumina-Forming Austenitic Steel in Molten Nitrate Salts by Gravimetric Analysis and Impedance Spectroscopy," *Materials and Corrosion* 65 (2014): 267–275, https://doi.org/10.1002/maco.201307422.

43. H. H. V. R. Dolling, A. Sterten, und, and R. Tunold, "Passivity and Pitting of Unalloyed Steel in Eutectic Sodium/Potassium Nitrite Melt," *Werkstoffe und Korrosion* 31 (1979): 470–474, https://doi.org/10.1002/maco.19800310607.

Appendix A
See Figures A1–A3.

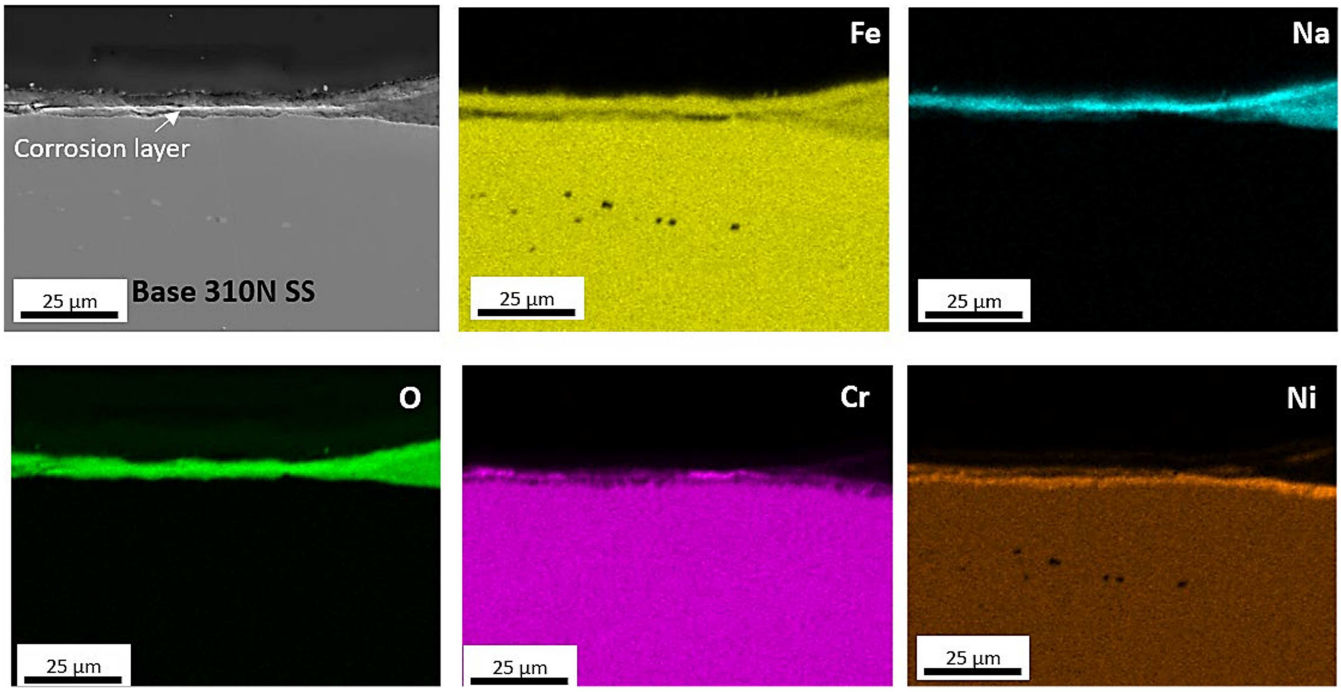

FIGURE A1 | SEM Cross-Section of 310N steel with respective EDX elemental maps obtained after 600 h of corrosion in solar salt at 600°C under 400 ppm NO with 80 vol% oxygen atmosphere. [Color figure can be viewed at wileyonlinelibrary.com]

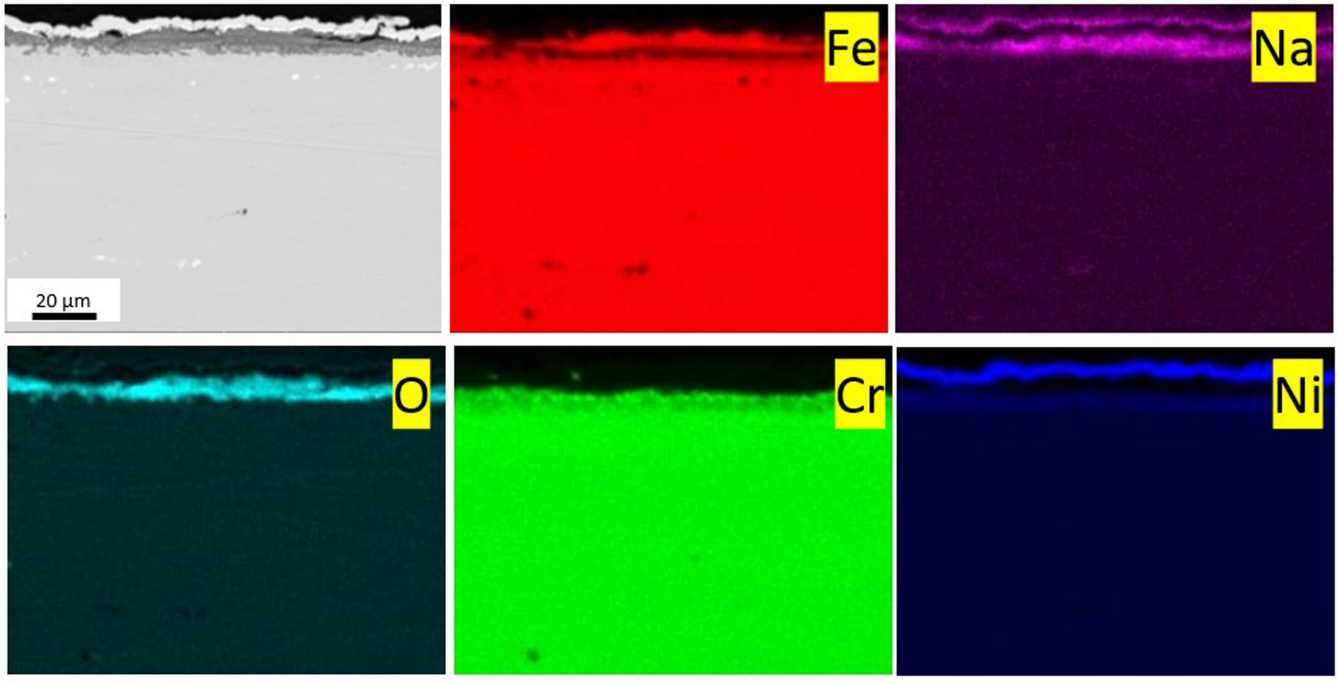

FIGURE A2 | SEM Cross-Section of 310N steel with respective EDX elemental maps obtained after 600 h of corrosion in solar salt at 600°C under 600 ppm NO with 60 vol% oxygen atmosphere. [Color figure can be viewed at wileyonlinelibrary.com]

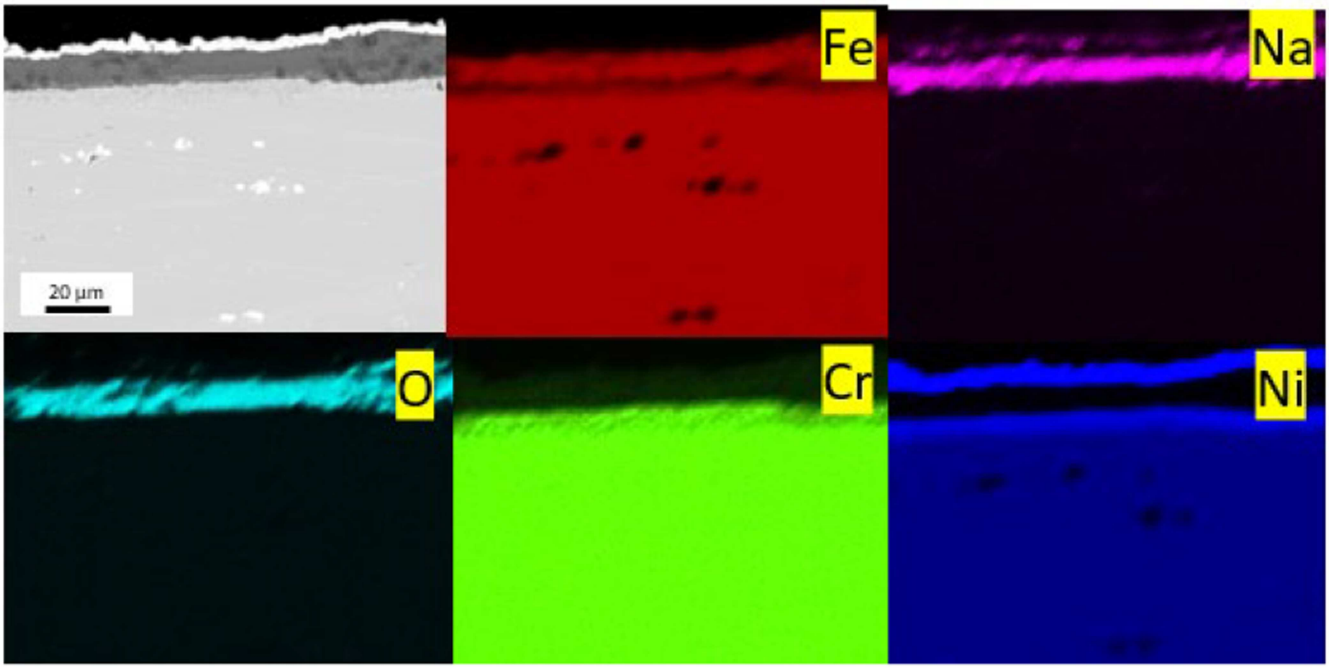

FIGURE A3 | SEM Cross-Section of 310N steel with respective EDX elemental maps obtained after 1224 h of corrosion in solar salt at 600°C under 600 ppm NO with 60 vol% oxygen atmosphere. [Color figure can be viewed at wileyonlinelibrary.com]